Zhang, H., Zhong, Z., Tang, R., Deng, X., Li, H., Wang, D. (2021): Modulation of Whistler Mode Waves by Ultra-Low Frequency Wave in a Macroscale Magnetic Hole: MMS Observations. - Geophysical Research Letters, 48, 22, e2021GL096056.

https://doi.org/10.1029/2021GL096056

AGU ADVANCING EARTH AND SPACE SCIENCE

Geophysical Research Letters®

RESEARCH LETTER
10.1029/2021GL096056

Key Points:

- We found whistler-mode waves and donut-shaped pitch angle distributions in a macroscale magnetic hole (MH)
- The formation of donut-shaped distribution is the result of the combined influence of MH and ultra-low frequency wave
- The butterfly distribution is considered to be the excitation mechanism of whistler-mode waves

Supporting Information:

Supporting Information may be found in the online version of this article.

Correspondence to:

R. Tang,
rongxint@ncu.edu.cn

Citation:

Zhang, H., Zhong, Z., Tang, R., Deng, X., Li, H., & Wang, D. (2021). Modulation of whistler mode waves by ultra-low frequency wave in a macroscale magnetic hole: MMS observations. *Geophysical Research Letters*, *48*, e2021GL096056. https://doi.org/10.1029/2021GL096056

Received 8 SEP 2021
Accepted 1 NOV 2021

Modulation of Whistler Mode Waves by Ultra-Low Frequency Wave in a Macroscale Magnetic Hole: MMS Observations

He Zhang[1,2], Zhihong Zhong[2,3], Rongxin Tang[2,4], Xiaohua Deng[2], Haimeng Li[2], and Dedong Wang[5]

[1]School of Resources Environmental and Chemical Engineering, Nanchang University, Nanchang, China, [2]Institute of Space Science and Technology, Nanchang University, Nanchang, China, [3]School of Materials Science and Engineering, Nanchang University, Nanchang, China, [4]Jiangxi Provincial Key Laboratory of Interdisciplinary Science, Nanchang University, Nanchang, China, [5]GFZ German Research Centre For Geosciences, Potsdam, Germany

Abstract We report the quasi-periodic whistler-mode waves corresponding to electron temperature anisotropy $T_{\perp}/T_{//} < 1$ at the center of a macroscale magnetic hole (MH) near the Earth's magnetopause observed by the Magnetospheric Multiscale mission. A significant ultra-low frequency (ULF) wave of background magnetic field was observed in this MH. The ULF wave dramatically exacerbates the evolution of MH and the formation of the donut-shaped electron pitch angle distribution (PAD) in the macroscale MH. When the whistler-mode waves were generated, they are consistent with troughs of the ULF wave and density increases, which is also related to the butterfly type PAD at those moments. The analysis of dispersion relation and cyclotron resonance condition indicate that whistler-mode waves were mainly generated by the butterfly type PAD of electrons. Our results provides new insights into one possible excitation mechanism of whistler-mode wave.

Plain Language Summary The whistler-mode wave is an important electromagnetic wave inside the magnetosphere. It is efficient for both the acceleration and precipitation of energetic electrons associated with typical magnetic field structures or boundaries. Moreover, the interactions between whistler-mode waves and other waves and corresponding wave generation mechanisms have attracted extensively attentions into data observations and computer simulations. In this study, we report an event of quasi-periodic whistler-mode waves and a background ultra-low frequency (ULF) wave at the center of a magnetic hole (MH), which has a negative electron temperature anisotropy $T_{\perp}/T_{\parallel} - 1 < 0$. The whistler-mode waves have the fluctuations in accordance with troughs of the ULF wave and were excited by the butterfly type pitch angle distribution. It indicates that the ULF wave can modulate the whistler-mode waves via bringing about the periodic variation of electron phase space density. The result exhibits the complicated processes of wave excitation and wave-particle interaction in the MH.

1. Introduction

The magnetic hole (MH), a quasi-stable magnetic structure characterized by the significant decreases of magnitude field, have been widely reported in solar wind (Turner et al., 1977), planetary magnetosphere (Balikhin et al., 2009; Burlaga et al., 1969; Volwerk et al., 2008), planetary magnetosheath (Goodrich et al., 2021; Wu et al., 2021), and comet (Russell et al., 1987). The scale size of MH covers from magneto-hydrodynamic-scale (Karlsson et al., 2021) to kinetic-scale (Huang et al., 2017). At present, it is generally accepted that the most popular formation mechanism of MH is the mirror instability (Ahmadi et al., 2017; Hasegawa, 1969; Southwood & Kivelson, 1993; T. Xiao et al., 2014). Moreover, some other mechanisms, such as slow solitons (Stasiewicz, 2004; Yao et al., 2016) and tearing instability (Balikhin et al., 2012) have been also considered.

Particle acceleration and abundant plasma wave activities have been observed in the MH, such as Langmuir waves (Lin et al., 1995), Alfvén waves (Tsurutani et al., 2002), and whistler-mode waves (Agapitov et al., 2020). Since plasma waves can efficiently convert energy and modulate the particle distribution (Bamber et al., 1994; Oka et al., 2017; Zhao et al., 2019), the study of the kinetic process and corresponding

wave-particle interactions in the MH can significantly improve our understanding of the energy conversion process in the plasma.

The excitation mechanism of whistler-mode waves is commonly considered to be the electron temperature anisotropy $T_{\perp}/T_{//} > 1$ (where $\perp$ and//are the perpendicular and parallel components to the background magnetic field) (Summers et al., 2009; Tang & Summers, 2012, 2019). Previous studies have shown that whistler waves are usually generated at the center or edge of the MH (Breuillard et al., 2018; Yao et al., 2019) and associated with the electron pancake pitch angle distribution (PAD; Peng et al., 2020; Zhima et al., 2015). Recently, Ahmadi et al. (2018) presented donut-shaped PAD associated with the generation process of whistler-mode waves, which is characterized by that the dominance of 90° electrons only appears near the edge of the MH, and the electron flux is strongest near the pitch angle of 45°/135° at the center of the MH. Although whistler-mode waves are observed with $T_{\perp}/T_{//} < 1$, Ahmadi et al. (2018) suggested that the whistler-mode waves generated were related to the electron temperature anisotropy at the edge of the MH. It should be noted that the donut-shaped PAD refers to the description of the periodic changes in the phase space density (PSD) of perpendicular electrons increasing or decreasing over a continuous period. In such a case, when we analyze the area where the PSD of the perpendicular pitch angles is reduced, the expression form of donut-shaped PAD is the same as the butterfly PAD.

However, the effects caused by the electron dynamics associated with the whistler-mode waves in MH are still inconclusive and most of the studies about the whistler waves are based on kinetic-scale MHs. The study of generation and features of whistler waves within macroscale MH still lacks. Here, we report an event of quasi-periodic emissions of whistler waves related to ultra-low frequency (ULF) waves within a macroscale MH observed by the Magnetospheric Multiscale (MMS) mission (Burch et al., 2016). The betatron cooling and trapping of the electrons by the ULF wave and MH form the quasi-periodic electron donut-shape PADs which are consistent with the emissions of whistler waves within this MH. The appearance of whistler waves corresponds to electron butterfly PADs (the center part of donut-shaped PAD). The detailed analysis of dispersion relation and cyclotron resonance condition can significantly demonstrate, for the first time, that the electron butterfly distribution can excite whistler-mode waves.

2. MMS Observations of Magnetic Hole

The MMS data used in this study are from the following instruments: the Fluxgate Magnetometer (Russell et al., 2016), the Search Coil Magnetometer (Le Contel et al., 2016), the Electric Double Probe (Ergun et al., 2016; Lindqvist et al., 2016), and the Fast Plasma Investigation (Pollock et al., 2016).

Figure 1 presents an overview of MMS1 observations from 06:10:00 to 06:30:00 UT on October 14, 2015. Figures 1a and 1b show the magnetic field components and the total magnetic field observed in the Geocentric Solar Magnetospheric coordinate system. The background magnetic field has a strong low-frequency disturbance. Figures 1c–1g give the electron density, ion velocity, ion temperature, ion energy spectrum, and electron energy spectrum, respectively. MMS1 observed an obvious magnetic structure during 06:15:00-06:16:00 UT (shadow area). The magnetic field at the edge of the structure slightly changes from [15, 35, 30] to [12, 40, 30] nT, while the magnetic field at the center is around [0.5, 10, 10] nT and the total magnetic field strength significantly decreases from 56 to 13 nT. We can estimate that the angle of the magnetic field changes 5.8° during this magnetic structure interval. Hence, we can identify this structure as a MH. Since the MMS1 was located at [8.8, 4.0, −2.2]R_e (Earth's radius), it indicates that this MH is near the Earth's magnetopause. It should be noted that, another decrease of the magnetic field and corresponding sudden decrease of the electron density were also observed by the MMS1 at 06:17:50 UT. At that moment, the minimum value of the total magnetic field is ~34.7nT which is significantly larger than the minimum magnetic field (~13 nT) in the MH. Furthermore, the ion temperature (Figure 1e) increases and the electron/ion fluxes (Figures 1f and 1g) change from strong to weak, which indicates that there was a magnetopause crossing with a northward interplanetary magnetic field. It further proves that, the magnetic field structure observed in the vicinity of 06:15:10 UT is a MH rather than a magnetopause's current sheet. Figures 1h–1m provide the zoom-in observations of the shadow area. This MH lasted for almost 40 s. Using the timing analysis method (Russell et al., 1983), we calculate the normal velocity as V_n ~60 km/s. Then, the size of the MH is about 2,400 km ~25.8di (1di ~93 km is the local ion inertia length). This is a typical macroscale

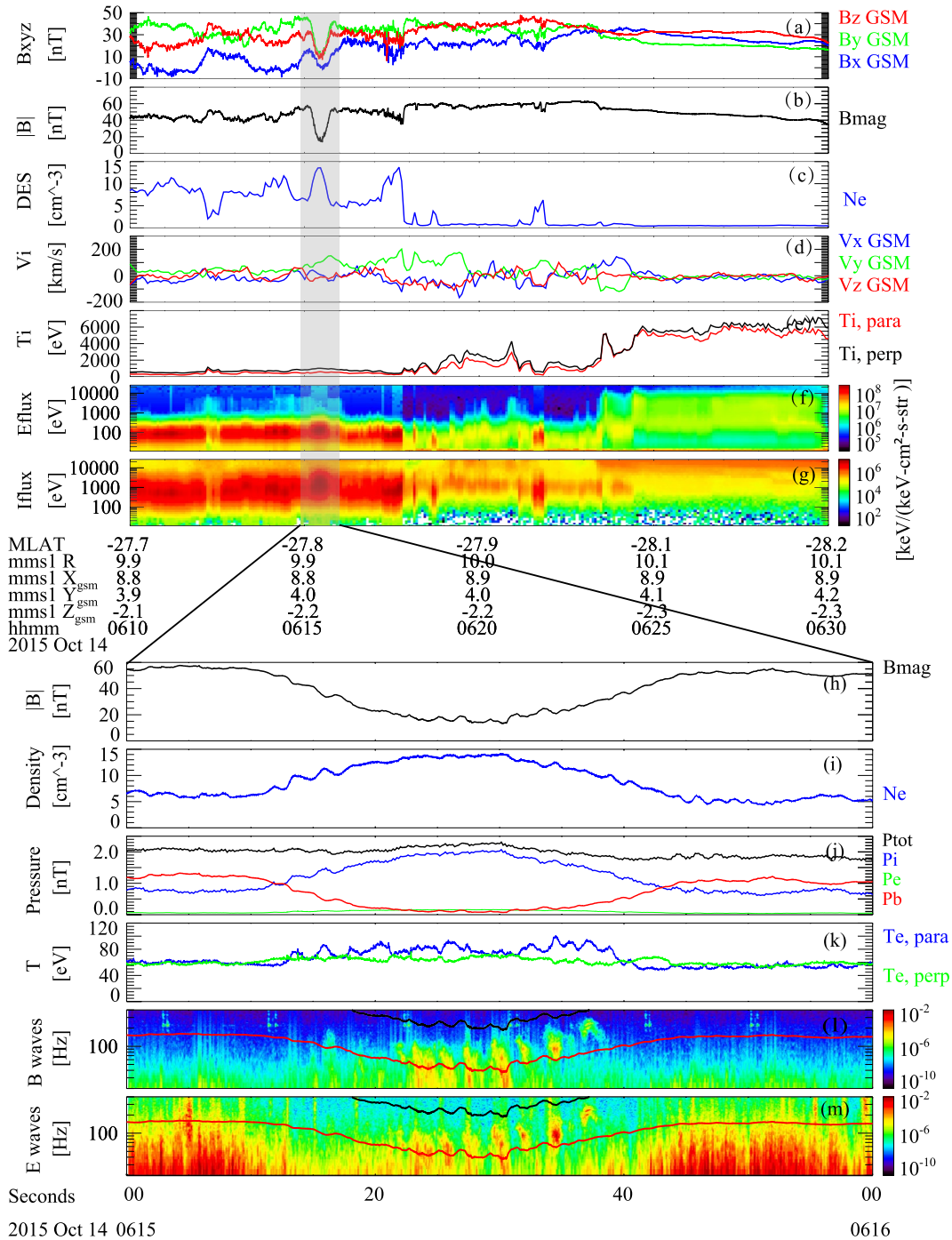

Figure 1. The overview of MMS1 observations. (a) Three components of magnetic field, (b) total magnetic field, (c) electron density, (d) ion velocity, (e) ion temperature, (f) ion and (g) electron differential energy fluxes. The gray shadow marks the macroscale magnetic hole (MH). Panels (h–m) are zoom-in MMS1 observations of the MH, with (h) total magnetic field; (i) electron density; (j) magnetic pressure (red), electron pressure (green), ion pressure (blue), and total pressure (black); (k) electron temperature; (l) magnetic and (m) electric field power spectral density (black and red solid lines represent 0.5fce and 0.1fce, respectively).

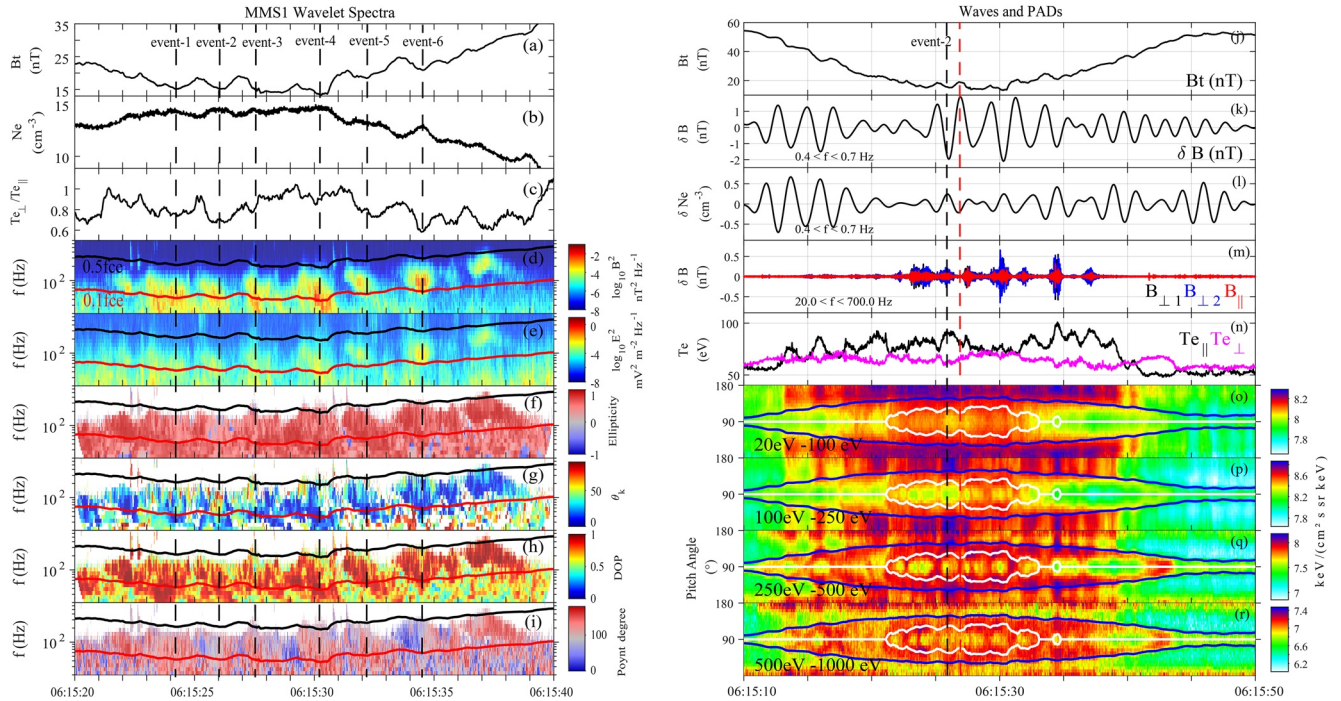

Figure 2. Waves and electron pitch angle distributions in the MH. Panels (a and j) are background magnetic field, (b) electron density, (c) electron temperature anisotropy, (d and e) magnetic and electric field power spectral density, (f) ellipticity, (g) wave normal angle, (h) degree of polarization, (i) Poynting flux, (k) ultra-low frequency wave with frequency 0.4 < f <0.7 Hz, (l) the electron density after bandpass filtering with frequency 0.4 < f <0.7 Hz, (m) the whistler-mode waveform with frequency 20 < f <700 Hz, (n) electron temperature. Electron pitch angle distributions in energy range (o) 20–100 eV, (p) 100–250 eV, (q) 250–500 eV, and (r) 500 eV–1.0 keV. The black and red solid lines represent 0.5fce and 0.1fce, respectively. The vertical dotted lines mark the whistler-mode waves events (left panels). The blue solid lines represent the MH trapping angle, and the white solid lines represent the trapping angle of the ultra-low frequency wave at the center of the MH. The vertical red and black dotted lines indicate one area without whistler-mode waves and one area of the whistler-mode wave with maximum wave intensity, respectively (right panels).

MH. As shown in Figure 1j, the increase of the ion pressure (red) and the decrease of the magnetic pressure (blue) result in an approximate balance of the total pressure (black) inside the MH. Furthermore, the electron temperature shows $T_{\perp}/T_{//} > 1$ at the edge of the MH, while the electron temperature shows $T_{\perp}/T_{//} < 1$ at the center of this MH (Figure 1k). Figures 1l and 1m give the magnetic field and the electric field power spectral density, respectively. Intense electromagnetic waves with the frequency around $0.1f_{ce}$ (red solid line, where f_{ce} represents the electron cyclotron frequency) and below $0.5f_{ce}$ (black solid line) were observed at the center of the MH.

Figures 2a–2i give the background magnetic field, electron density, electron temperature anisotropy, and the polarization analysis of electromagnetic waves at the canter of the MH from 06:15:20 to 06:15:40 UT, which are calculated by the singular value decomposition method (Santolík et al., 2003). The black and red solid lines in Figures 2d–2j also represent $0.5f_{ce}$ and $0.1f_{ce}$, respectively. The spectrums show that these electromagnetic waves are discrete. Since they have quasi-periodic emission, right-handed polarization, and propagation angles about 0° ~ 30°, we can determine that these waves are the whistler-mode waves. Those black dotted lines mark six typical whistler-mode waves at the center of the MH. It can be noted that, the Poynting flux (Figure 2i) shows both parallel and anti-parallel propagations corresponding to the background magnetic field within the MH. This generally means that there is likely to be the excitation source of these whistler-mode waves. Generally, it is believed that the excitation mechanisms of whistler-mode waves are mostly associated with the electron temperature anisotropy via electron cyclotron resonance (Summers & Tang, 2021; Summers et al., 2011, 2013; Tang et al., 2014; Zhang et al., 2020; Zhou et al., 2013) or electron beams through Landau resonance (An et al., 2017; Hsieh & Omura, 2018; Mourenas et al., 2015). However, in this case, the electron parallel temperature is clearly greater than the perpendicular temperature at the center of this MH (Figure 2c). Besides, these whistler-mode waves correspond to the decrease of electron temperature anisotropy and the small cavities of the background magnetic field within the MH.

Figures 2j–2r presents further details of waves and electron PADs in the MH. We firstly performed the Fast Fourier Transform on the total background magnetic field (Figure 2j), and the results show that the background magnetic field disturbance has a significantly higher power spectral density in the frequency range of 0.4–0.7 Hz, which is close to the ion cyclotron frequency (see Figure S1 in Supporting Information S1). Then, Figures 2k and 2l give the low-frequency fluctuations of the background magnetic field and the electron density after bandpass filtering with frequency $0.4 < f < 0.7$ Hz. It can be seen that, the ULF wave in the background magnetic field persists in the whole MH (Figure 2k) and there is a negative correlation between the fluctuation of the electron density and this ULF wave. Using the timing analysis we find that the normal direction of the ULF wave is about [0.85, 0.39, and 0.37] corresponding to the wave normal angle ~ 68° and the phase velocity is ~212 km/s. The plasma velocity V_i in the MH is ~52 km/s in the wave normal direction, indicating that the propagation velocity of the ULF wave is much faster than the convection velocity of the ambient plasma. Furthermore, the parallel velocity of this ULF wave can be estimated based on the electron bulk velocity and magnetic field. We then selected the time interval 06:15:30–06:15:40 UT when the intensities of whistler-mode waves are strong enough to obtain the local Alfvén speed and the parallel velocity of the ULF wave, where $B = 25$ nT and $n = 12$ cm^{-3}. The estimated local Alfvén speed is $V_A = B/\sqrt{\mu_0 m_{H^+} n_{H^+}} = 157$ km/s, where μ_0 is the vacuum magnetic permeability, n_{H^+} is the number density of H^+ and m_{H^+} is the mass of H^+. The correlation coefficient of $\Delta Ve_\perp$ (perpendicular bulk velocity after bandpass filtering) and $\Delta B_\perp$ (perpendicular magnetic fields after bandpass filtering) is 0.6 by using $\Delta Ve_\perp = -(\omega/k_\parallel)\Delta B_\perp/B$ (Gershman et al., 2017). In such a case, the corresponding parallel velocity of the ULF wave finally appears as $\omega/k_\parallel = 1.34 \pm 0.1 V_A$, which is consistent with the result from the timing analysis. Therefore, this ULF wave is more likely the Alfvén wave and propagates parallel to the background magnetic field.

The electron PADs from 20 eV to 1 keV associated with the ULF wave are shown in Figures 2o–2r where blue lines are the trapping angle θ and $180° - \theta$ calculated by the function $\theta = \arcsin(\sqrt{|B|/|B_{\max}|})$ (Breuillard et al., 2018), where B is the minimum value of total magnetic field in the MH, and $B_{\max}$ is the maximum value of total magnetic field at the edge of the MH. The white lines are also the trapping angles calculated from the decreasing magnetic field due to the ULF wave. Here, B is the minimum value of the local magnetic field caused by the ULF wave (at the troughs of ULF wave), and $B_{\max}$ is the maximum magnetic field at the edge of the locally reduced magnetic field (which corresponds to the peaks of ULF wave). Generally, those electrons with a pitch angle between two blue lines can be trapped within the mirror structure of the MH. The electrons around pitch angle $\alpha = 90°$ become deeply trapped by the MH mirror structure, which is also trapped by the mirror structures caused by the ULF wave. For the energy range of 20–100 eV, parallel and antiparallel electrons are dominated. Only a small fraction of electrons near $\alpha = 90°$ are trapped while most of the electrons under this energy range are not trapped in the MH. For the energy range of 100–250 eV, 90° electrons are gradually trapped. Moreover, more perpendicular electrons have been significantly trapped at the energy ranges of 250–500 and 500–1,000 eV, while the electrons with the pitch angle nearly 90° are cooled as the background magnetic field becomes smaller. In such a case, electron distributions are shown as donut-shaped pitch angle distributions. The above characteristics are especially obvious for energetic electrons at the ranges of 100–250 and 250–500 eV. Interestingly, we find that the drops of the magnetic field dramatically correspond to the troughs of the ULF wave. In addition, all peaks and troughs of the ULF wave are significantly consistent with the decreases and increases of electrons with $\alpha = 90°$, respectively. It suggests that, the ULF wave has a certain modulation effect on the PADs of energetic electrons from 100 to 500 eV inside the MH, which is likely to affect the cooling of deeply trapped electrons and the formation of the donut-shaped electron distribution.

Moreover, it is worth further investigating the excitation of whistler-mode waves in the right panels of Figure 2, the red dotted line indicates one of the areas where no whistler-mode waves are observed. Whereas, the black dotted line indicates the event-2 with significant electron parallel temperature higher than electron perpendicular temperature among several whistler-mode waves events. We can then check the detailed differences of corresponding background parameters by comparisons with and without the whistler-mode wave. The appearance of whistler-mode waves corresponds to the trough of the ULF wave, and the electron PAD clearly shows the absence of 90° electrons in the donut-shaped PAD. The areas without whistler waves correspond to the peaks of the ULF wave and the increase of 90° electrons.

Figure 3 presents the relationship between the power spectral density of whistler-mode waves, electron PAD, and cyclotron resonance energies. Figures 3a–3c and show the power spectral density of whistler waves for six typical whistler-mode emissions (from event-1 to event-6). Taking event-1 (Figure 3a) as an example, the PSD clearly indicates that the wave has been significantly enhanced in the frequency range from 23 to 103 Hz. The vertical lines mark the wave frequencies corresponding to the beginning (blue line), peak (orange line), and end (purple line) of the power spectrum intensity of this whistler wave. In addition, the power spectral density of other wave events (Figures 3b, 3c and 3g–3i) also have enhancements in different frequency ranges, and those corresponding frequencies are all marked. We give the correlations between the cyclotron resonance energies and the electron PADs as shown in Figures 3d–3f and 3j–3l. It can be noted that electrons present the field-aligned PADs at the low energy (<200 eV) for all six wave events. The electron PSDs with higher energies (>200 eV) near 45°/135° are significantly larger than those PSDs near 0°/90°/180° sindicating the typical butterfly shaped distribution. Furthermore, using the formula $V_{res} = (\omega - \Omega_{ce})/k_{\|}$ and $k_{\|}^2 = (\omega^2 - \omega \times \omega_{pe}^2/(\omega - \Omega_{ce}))/c^2$ (Kitamura et al., 2020), we can calculate the cyclotron resonance velocities of the whistler-mode waves, where ω is the angular frequency of the waves, $k_{\|}$ is the wave number in the parallel direction, c is the light speed, and ω_{pe} is the electron plasma frequency. Here, B and N_e are the average magnetic field and the average electron density during the time interval of each wave event. We use the wave frequencies marked in the power spectral density (Figures 3a–3c and 3g–3i) to obtain the corresponding minimum resonance energies via $E_{res} = \frac{1}{2} m_e {V_{res}}^2$. The dotted solid lines in Figures 3d–3f and plot the minimum resonance energies corresponding to the beginning, peak, and end frequencies of whistler-mode waves. For example, in Figure 3d, the energy range of the butterfly PAD is clearly within the electron cyclotron resonance energy of this whistler wave. In particular, the resonance energy at the peak of the power spectral density (orange line) coincides with the enhancement of 45°/135° energetic electrons. The calculated minimum resonance energies are approximately [100–1,000]eV, which is also consistent with the energy range of the donut-shaped PADs in Figures 2p–2r. These above characteristics are still shown in other wave events (Figures 3e, 3f and 3j–3l), which can effectively prove that the whistler-mode waves and the electrons within the energy range of buttery PADs have cyclotron resonance.

Since whistler-mode waves correspond to the obvious negative temperature anisotropy at 06:15:26 UT (event-2, the black dotted line in Figure 2), we select the energy range with obvious butterfly PAD to carry out the PSD fitting using multiple component bi-Maxwellian distribution (Figure 4a). The fitting parameters of nine electron components are listed in Table S1 in Supporting Information S1. We further evaluate the growth rates of the whistler-mode wave for the event-2 from the Waves in Homogeneous Anisotropic Multicomponent Magnetized Plasma (WHAMP) (Rönnmark, 1982). As shown in Figures 4b and 4c, a significant positive wave growth with a maximum rate $\gamma/\omega_{ce} = 0.01$ is consistent with the right-handed polarization occurring at normalized frequency ω/ω_{ce} ~0.1, which is consistent with the observed wave frequency ($0.1f_{ce}$) in event-2 of Figure 2d. The predicted results suggest that whistler-mode waves can be driven by the butterfly PAD in this event through electron cyclotron resonance.

Similarly, we also select the area without whistler-mode wave (the red dotted line in left panels of Figure 2) to perform corresponding fittings of the electron PSD and calculate the whistler wave growth rate, as shown in Figures 4d–4f. The fitting parameters are listed in Table S2 in Supporting Information S1. It can be seen that, compared with Figures 4a–4c, the PSD of perpendicular electrons slightly increases, while the electron PSDs around 45 and 135 slightly decrease. Meanwhile, the dispersion relationship shows no positive wave growth rate at this moment and the whistler-mode wave can not be generated. To further validate the whistler-mode wave generation, we give more results of the PSD fittings and the growth rate calculations for the whistler-mode wave events 1, 4 and 6 (the areas with and without whistler-mode waves) in Figures S2, S3 and S4 in Supporting Information S1. The fitting parameters are listed in Tables S3–S7 in Supporting Information S1. Although the anti-propagation characteristics are more obvious in Poynting flux for some events (event-1 and event-4), it may be related to the trajectory of the MMS. The subtle forward propagation properties can still be seen in the local magnetic field decrease areas (or called the whistler-mode wave duration). All the above observation characteristics and theoretical calculations further indicate that the whistler-mode waves can be driven by the electron butterfly PAD through cyclotron resonance.

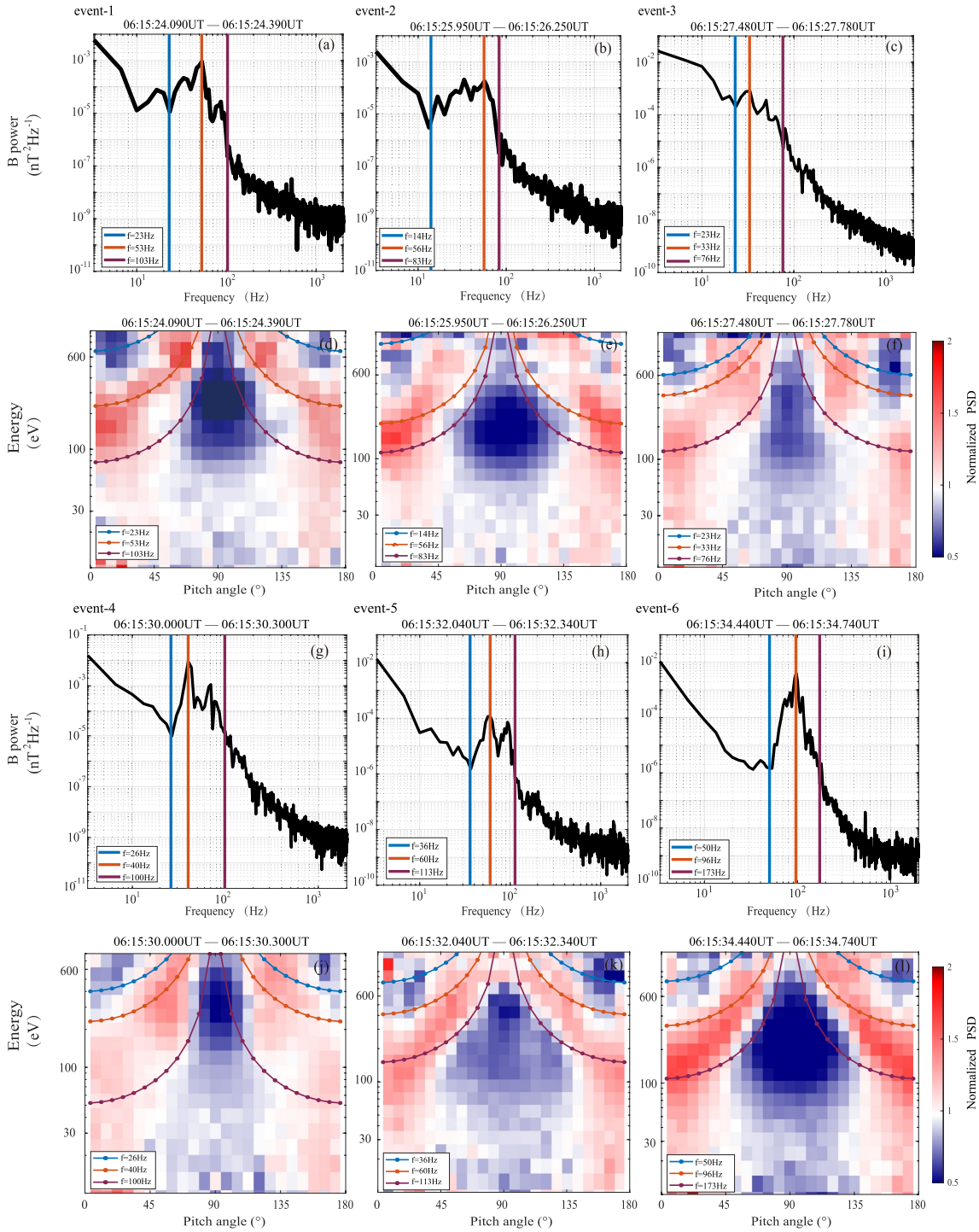

Figure 3. The power spectral densities of six whistler events and corresponding electron pitch angle distributions (PADs). Panels (a–c and g–i) are the power spectral density of the whistler-mode waves. The vertical lines represent the corresponding frequency of the wave's power spectral density at the beginning, peak, and end, respectively. Panels (d–f and j–l) are PADs of different energy electrons. The colorbars present the normalized electron phase space density (PSD), which was calculated by the average electron PSDs in different pitch angles of each energy and normalized by the electron PSDs in each pitch angle bin to the average value of the PSDs. The dot solid lines with different colors represent the cyclotron resonance energies at different frequencies, where the frequencies used are obtained in the panels (a–c and g–i).

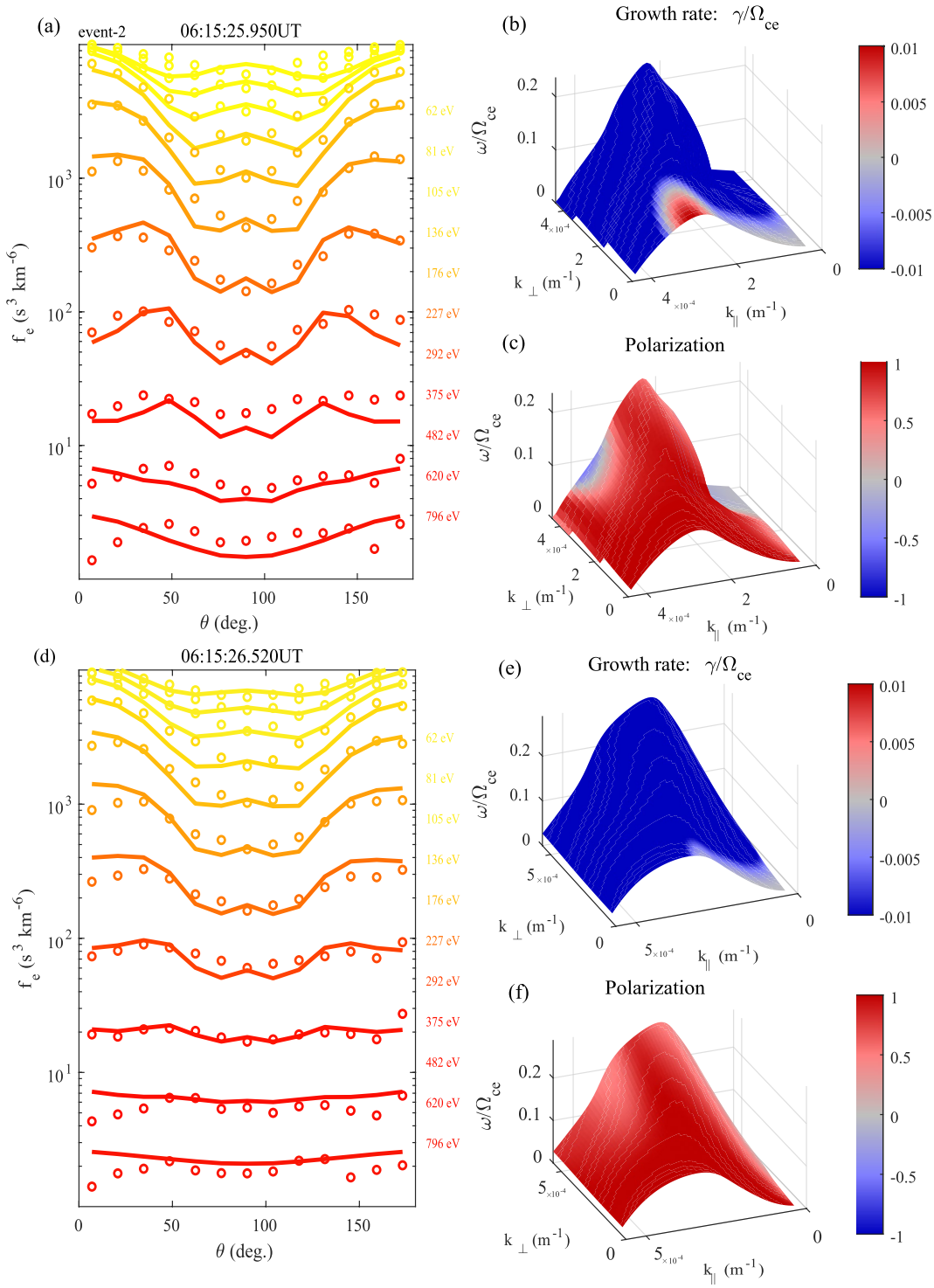

Figure 4. The electron phase density and wave growth rate of (a–c) event-2 at 06:15:26 UT and (d–f) the area without whistler-mode wave at 06:15:26.52 UT. Panels (a and d) are the electron phase space density, where the solid line represents the fitting value and the circle represents the observed value. Panels (b and e) are the predicted dispersion surface of the whistler-mode wave. Panels (c) and (f) are the predicted polarization of the whistler-mode wave.

3. Conclusions

We report a case study of the modulation relationship between a ULF wave and the whistler-mode waves observed inside a macroscale MH in the Earth's magnetopause. The electron PADs in the MH present the donut-shaped distribution, and whistler-mode waves are always generated corresponding to the ULF wave troughs and butterfly distributions. The donut-shaped PAD is mainly formed due to the betatron cooling during the evolution of the MH (Ahmadi et al., 2018; Yao et al., 2018; Z. Li, 2020). As for our case, at the beginning, the MH has preliminarily trapped the electrons within the trapping angle due to the magnetic mirror effect. Then, the existence of the ULF wave aggravated the deepening of the MH (decreased the background magnetic field in the macroscale scale), strengthened the betatron cooling effect, and leaded to the reduction of 90° electrons. However, most of these perpendicular electrons reduced by the betatron cooling from the ULF wave are still trapped inside the MH. In such a case, the ULF wave is the main reason to form the donut-shaped PAD inside this macroscale MH. However, when we particularly concentrate on the donut-shaped PAD where the whistler wave is generated, the electron PAD clearly shows a butterfly distribution at this moment. Although the electron temperature has primarily negative anisotropy ($T_{\perp}/T_{//} < 1$), it has been confirmed by WHAMP that the unstable butterfly distribution provides the free energy to excite the whistler waves at the minimum magnetic field inside the MH.

Furthermore, in the Earth's magnetosphere, the butterfly PAD is very common (H. Li et al., 2020; Ni et al., 2020, 2016), and a statistical study presents that the occurrence rate of electron butterfly PADs is related to the magnetic dips in near-Earth space (Xiong et al., 2019). However, the wave-particle interaction related to the formation of butterfly shaped distribution is still controversial. In the Earth's radiation belt, butterfly PADs have been suggested can be caused by the combined acceleration by whistler-mode chorus wave and magnetosonic (MS) wave (F. Xiao et al., 2015), the Landau resonance with MS wave (J. Li et al., 2016), or the Landau/cyclotron resonance with whistler-mode hiss wave (Albert et al., 2016). For the first time, our study successfully demonstrates that the butterfly PAD can generate whistler-mode waves inside a macroscale MH, which can dramatically aid in the understandings of whether and how the butterfly PADs in space plasma contribute to the excitation of whistler-mode waves, as well as the wave-particle interactions, wave coupling, and corresponding electron kinetics etc.

Data Availability Statement

The spacecraft Data used for this study are publicly available from the MMS Science Data Center (https://lasp.colorado.edu/mms/sdc/public/about/browse-wrapper/).

Acknowledgments
The authors thank the entire MMS team and MMS Science Data Center for providing the high-quality data for this study. This work was supported by the National Natural Science Foundation of China under grants 41974195 and 42130211, the Project funded by the China Postdoctoral Science Foundation grant 2021M691395, and the Interdisciplinary Innovation Fund of Natural Science from the Nanchang University under grant 9166-27060003-YB14.

References

Agapitov, O. V., de Wit, T. D., Mozer, F. S., Bonnell, J. W., Drake, J. F., Malaspina, D., et al. (2020). Sunward-propagating whistler waves collocated with localized magnetic field holes in the solar wind: Parker solar probe observations at 35.7 $R_{\odot}$ radii. *The Astrophysical Journal*, *891*(1), L20. https://doi.org/10.3847/2041-8213/ab799c

Ahmadi, N., Germaschewski, K., & Joachim, R. (2017). Simulation of magnetic holes formation in the magnetosheath. *Physics of Plasmas*, *24*(12), 122121. https://doi.org/10.1063/1.5003017

Ahmadi, N., Wilder, F. D., Ergun, R. E., Argall, M., Usanova, M. E., Breuillard, H., et al. (2018). Generation of electron whistler waves at the mirror mode magnetic holes: MMS observations and PIC simulation. *Journal of Geophysical Research: Space Physics*, *123*(8), 6383–6393. https://doi.org/10.1029/2018JA025452

Albert, J. M., Starks, M. J., Horne, R. B., Meredith, N. P., & Glauert, S. A. (2016). Quasi-linear simulations of inner radiation belt electron pitch angle and energy distributions. *Geophysical Research Letters*, *43*(6), 2381–2388. https://doi.org/10.1002/2016GL067938

An, X., Bortnik, J., Van Compernolle, B., Decyk, V., & Thorne, R. (2017). Electrostatic and whistler instabilities excited by an electron beam. *Physics of Plasmas*, *24*(7), 072116. https://doi.org/10.1063/1.4986511

Balikhin, M. A., Sagdeev, R. Z., Walker, S. N., Pokhotelov, O. A., Sibeck, D. G., Beloff, N., & Dudnikova, G. (2009). Themis observations of mirror structures: Magnetic holes and instability threshold. *Geophysical Research Letters*, *36*(3). https://doi.org/10.1029/2008GL036923

Balikhin, M. A., Sibeck, D. G., Runov, A., & Walker, S. N. (2012). Magnetic holes in the vicinity of dipolarization fronts: Mirror or tearing structures? *Journal of Geophysical Research*, *117*(A08229). https://doi.org/10.1029/2012JA017552

Bamber, J. F., Gekelman, W., & Maggs, J. E. (1994). Whistler wave mode conversion to lower hybrid waves at a density striation. *Physical Review Letters*, *73*, 2990–2993. https://doi.org/10.1103/PhysRevLett.73.2990

Breuillard, H., LeContel, O., Chust, T., Berthomier, M., Retino, A., Turner, D. L., et al. (2018). The properties of lion roars and electron dynamics in mirror mode waves observed by the Magnetospheric Multiscale Mission. *Journal of Geophysical Research: Space Physics*, *123*(1), 93–103. https://doi.org/10.1002/2017JA024551

Burch, J., Moore, T., Torbert, R., & Giles, B. (2016). Magnetospheric Multiscale overview and science objectives. *Space Science Reviews*, *199*(1–4), 5–21. https://doi.org/10.1007/s11214-015-0164-9

Burlaga, L., Ogilvie, K., & Fairfield, D. (1969). Microscale fluctuations in the interplanetary magnetic field. *The Astrophysical Journal*, *155*, L171. https://doi.org/10.1086/180329

Ergun, R. E., Tucker, S., Westfall, J., Goodrich, K. A., Malaspina, D. M., Summers, D., et al. (2016). The axial double probe and fields signal processing for the MMS mission. *Space Science Reviews*, *199*(1–4), 167–188. https://doi.org/10.1007/s11214-014-0115-x

Gershman, D. J., Adolfo, F., Dorelli, J. C., Boardsen, S. A., Avanov, L. A., Bellan, P. M., et al. (2017). Wave-particle energy exchange directly observed in a kinetic Alfvén-branch wave. *Nature Communications*, *8*(1), 1–10. https://doi.org/10.1038/ncomms14719

Goodrich, K. A., Bonnell, J. W., Curry, S., Livi, R., Whittlesey, P., Mozer, F., et al. (2021). Evidence of subproton-scale magnetic holes in the Venusian magnetosheath. *Geophysical Research Letters*, *48*(5), e2020GL090329. https://doi.org/10.1029/2020GL090329

Hasegawa, A. (1969). Drift mirror instability in the magnetosphere. *The Physics of Fluids*, *12*(12), 2642–2650. https://doi.org/10.1063/1.1692407

Hsieh, Y.-K., & Omura, Y. (2018). Nonlinear damping of oblique whistler mode waves via Landau resonance. *Journal of Geophysical Research: Space Physics*, *123*(9), 7462–7472. https://doi.org/10.1029/2018JA025848

Huang, S. Y., Du, J. W., Sahraoui, F., Yuan, Z. G., He, J. S., Zhao, J. S., et al. (2017). A statistical study of kinetic-size magnetic holes in turbulent magnetosheath: MMS observations. *Journal of Geophysical Research: Space Physics*, *122*(8), 8577–8588. https://doi.org/10.1002/2017JA024415

Karlsson, T., Heyner, D., Volwerk, M., Morooka, M., Plaschke, F., Goetz, C., & Hadid, L. (2021). Magnetic holes in the solar wind and magnetosheath near mercury. *Journal of Geophysical Research: Space Physics*, *126*(5), e2020JA028961. https://doi.org/10.1029/2020JA028961

Kitamura, N., Omura, Y., Nakamura, S., Amano, T., Boardsen, S., Ahmadi, N., et al. (2020). Observations of the source region of whistler mode waves in magnetosheath mirror structures. *Journal of Geophysical Research: Space Physics*, *125*(5), e2019JA027488. https://doi.org/10.1029/2019ja027488

Le Contel, O., Leroy, P., Roux, A., Coillot, C., Alison, D., Bouabdellah, A., et al. (2016). The search-coil magnetometer for MMS. *Space Science Reviews*, *199*(1–4), 257–282. https://doi.org/10.1007/s11214-014-0096-9

Li, H., Peng, Q., Tang, R., Zhang, H., Zhong, Z., Deng, X., & Wang, D. (2020). Statistical characteristics of electron pitch angle distributions inside the magnetopause based on MMS observations. *Journal of Geophysical Research: Space Physics*, *125*(10), e2020JA028291. https://doi.org/10.1029/2020JA028291

Li, J., Ni, B., Ma, Q., Xie, L., Pu, Z., Fu, S., et al. (2016). Formation of energetic electron butterfly distributions by magnetosonic waves via Landau resonance. *Geophysical Research Letters*, *43*(7), 3009–3016. https://doi.org/10.1002/2016GL067853

Li, Z. (2020). In situ evidence of a magnetic hole downstream of the magnetic reconnection in the magnetopause reconnection. *The Astrophysical Journal*, *901*(1), 20. https://doi.org/10.3847/1538-4357/abad33

Lin, N., Kellogg, P., MacDowall, R., Balogh, A., Forsyth, R., Phillips, J., et al. (1995). Observations of plasma waves in magnetic holes. *Geophysical Research Letters*, *22*(23), 3417–3420. https://doi.org/10.1029/95GL03266

Lindqvist, P.-A., Olsson, G., Torbert, R., King, B., Granoff, M., Rau, D., et al. (2016). The spin-plane double probe electric field instrument for MMS. *Space Science Reviews*, *199*(1–4), 137–165. https://doi.org/10.1007/s11214-014-0116-9

Mourenas, D., Artemyev, A., Agapitov, O., Krasnoselskikh, V., & Mozer, F. (2015). Very oblique whistler generation by low-energy electron streams. *Journal of Geophysical Research: Space Physics*, *120*(5), 3665–3683. https://doi.org/10.1002/2015JA021135

Ni, B., Yan, L., Fu, S., Gu, X., Cao, X., Xiang, Z., & Zhang, Y. (2020). Distinct formation and evolution characteristics of outer radiation belt electron butterfly pitch angle distributions observed by Van Allen Probes. *Geophysical Research Letters*, *47*(4), e2019GL086487. https://doi.org/10.1029/2019GL086487

Ni, B., Zou, Z., Li, X., Bortnik, J., Xie, L., & Gu, X. (2016). Occurrence characteristics of outer zone relativistic electron butterfly distribution: A survey of Van Allen Probes REPT measurements. *Geophysical Research Letters*, *43*(11), 5644–5652. https://doi.org/10.1002/2016GL069350

Oka, M., Wilson, L. B. W., III, Phan, T. D., Hull, A. J., Amano, T., Hoshino, M., et al. (2017). Electron scattering by high-frequency whistler waves at earth's bow shock. *The Astrophysical Journal Letters*, *842*(2), L11. https://doi.org/10.3847/2041-8213/aa7759

Peng, Q., Li, H., Tang, R., Zhong, Z., Zhang, H., & Li, Q. (2020). Variation of dayside chorus waves associated with solar wind dynamic pressure based on MMS observations. *Advances in Space Research*, *65*(11), 2551–2558. https://doi.org/10.1016/j.asr.2020.03.006

Pollock, C., Moore, T., Jacques, A., Burch, J., Gliese, U., Saito, Y., et al. (2016). Fast plasma investigation for Magnetospheric Multiscale. *Space Science Reviews*, *199*(1–4), 331–406. https://doi.org/10.1007/s11214-016-0245-4

Rönnmark, K. (1982). *Whamp-waves in homogeneous, anisotropic, multicomponent plasmas* (Technical Report, pp. 1–55). Kiruna Geophysical Institute.

Russell, C., Anderson, B., Baumjohann, W., Bromund, K., Dearborn, D., Fischer, D., et al. (2016). The Magnetospheric Multiscale magnetometers. *Space Science Reviews*, *199*(1–4), 189–256. https://doi.org/10.1007/s11214-014-0057-3

Russell, C., Gosling, J. T., Zwickl, R. D., & Smith, E. J. (1983). Multiple spacecraft observations of interplanetary shocks: ISEE three-dimensional plasma measurements. *Journal of Geophysical Research*, *88*(A12), 9941–9947. https://doi.org/10.1029/JA088iA12p09941

Russell, C., Riedler, W., Schwingenschuh, K., & Yeroshenko, Y. (1987). Mirror instability in the magnetosphere of comet Halley. *Geophysical Research Letters*, *14*(6), 644–647. https://doi.org/10.1029/GL014i006p00644

Santolík, O., Parrot, M., & Lefeuvre, F. (2003). Singular value decomposition methods for wave propagation analysis. *Radio Science*, *38*(1). https://doi.org/10.1029/2000RS002523

Southwood, D. J., & Kivelson, M. G. (1993). Mirror instability: 1. Physical mechanism of linear instability. *Journal of Geophysical Research*, *98*(A6), 9181–9187. https://doi.org/10.1029/92JA02837

Stasiewicz, K. (2004). Theory and observations of slow-mode solitons in space plasmas. *Physical Review Letters*, *93*(12), 125004. https://doi.org/10.1103/PhysRevLett.93.125004

Summers, D., & Tang, R. (2021). Influence of kappa distributions on the whistler mode instability. *Journal of Geophysical Research: Space Physics*, *126*(1), e2020JA028276. https://doi.org/10.1029/2020JA028276

Summers, D., Tang, R., & Omura, Y. (2011). Effects of nonlinear wave growth on extreme radiation belt electron fluxes. *Journal of Geophysical Research*, *116*(A10). https://doi.org/10.1029/2011JA016602

Summers, D., Tang, R., Omura, Y., & Lee, D.-H. (2013). Parameter spaces for linear and nonlinear whistler-mode waves. *Physics of Plasmas*, *20*(7), 072110. https://doi.org/10.1063/1.4816022

Summers, D., Tang, R., & Thorne, R. M. (2009). Limit on stably trapped particle fluxes in planetary magnetospheres. *Journal of Geophysical Research*, *114*(A10). https://doi.org/10.1029/2009JA014428

Tang, R., & Summers, D. (2012). Energetic electron fluxes at Saturn from Cassini observations. *Journal of Geophysical Research*, *117*(A6). https://doi.org/10.1029/2011JA017394

Tang, R., & Summers, D. (2019). Dependence of whistler mode chorus wave generation on the maximum linear growth rate. *Journal of Geophysical Research: Space Physics*, *124*(6), 4114–4124. https://doi.org/10.1029/2018JA026413

Tang, R., Summers, D., & Deng, X. (2014). Effects of cold electron number density variation on whistler-mode wave growth. *Annales Geophysicae*, *32*, 889–898. https://doi.org/10.5194/angeo-32-889-2014

Tsurutani, B., Galvan, C., Arballo, J., Winterhalter, D., Sakurai, R., Smith, E., et al. (2002). Relationship between discontinuities, magnetic holes, magnetic decreases, and nonlinear Alfvén waves: Ulysses observations over the solar poles. *Geophysical Research Letters*, *29*(11), 23-1–23-4. https://doi.org/10.1029/2001GL013623

Turner, J. M., Burlaga, L. F., Ness, N. F., & Lemaire, J. F. (1977). Magnetic holes in the solar wind. *Journal of Geophysical Research*, *82*(13), 1921–1924. https://doi.org/10.1029/JA082i013p01921

Volwerk, M., Zhang, T. L., Delva, M., Vörös, Z., Baumjohann, W., & Glassmeier, K.-H. (2008). Mirror-mode-like structures in Venus' induced magnetosphere. *Journal of Geophysical Research*, *113*(E9). https://doi.org/10.1029/2008JE003154

Wu, M., Chen, Y., Du, A., Wang, G., Xiao, S., Peng, E., et al. (2021). Statistical properties of small-scale linear magnetic holes in the Martian magnetosheath. *The Astrophysical Journal*, *916*(2), 104. https://doi.org/10.3847/1538-4357/ac090b

Xiao, F., Yang, C., Su, Z., Zhou, Q., He, Z., He, Y., et al. (2015). Wave-driven butterfly distribution of Van Allen belt relativistic electrons. *Nature Communications*, *6*(1), 1–9. https://doi.org/10.1038/ncomms9590

Xiao, T., Shi, Q., Tian, A., Sun, W., Zhang, H., Shen, X., et al. (2014). Plasma and magnetic-field characteristics of magnetic decreases in the solar wind at 1 AU: *Cluster*-C1 observations. In *Coronal magnetometry* (pp. 553–573). Springer. https://doi.org/10.1007/978-1-4939-2038-9_32

Xiong, Y., Xie, L., Fu, S., & Pu, Z. (2019). Statistical study of energetic electron butterfly pitch angle distributions during magnetic dip events. *Geophysical Research Letters*, *46*(23), 13621–13629. https://doi.org/10.1029/2019GL085091

Yao, S. T., Shi, Q. Q., Li, Z. Y., Wang, X. G., Tian, A. M., Sun, W. J., et al. (2016). Propagation of small size magnetic holes in the magnetospheric plasma sheet. *Journal of Geophysical Research: Space Physics*, *121*(6), 5510–5519. https://doi.org/10.1002/2016JA022741

Yao, S. T., Shi, Q. Q., Liu, J., Yao, Z. H., Guo, R. L., Ahmadi, N., et al. (2018). Electron dynamics in magnetosheath mirror-mode structures. *Journal of Geophysical Research: Space Physics*, *123*(7), 5561–5570. https://doi.org/10.1029/2018JA025607

Yao, S. T., Shi, Q. Q., Yao, Z. H., Li, J. X., Yue, C., Tao, X., et al. (2019). Waves in kinetic-scale magnetic dips: MMS observations in the magnetosheath. *Geophysical Research Letters*, *46*(2), 523–533. https://doi.org/10.1029/2018GL080696

Zhang, H., Li, Q., Tang, R., Li, H., Wang, D., Chen, Z., & Deng, X. (2020). Background parameter effects on linear–nonlinear chorus wave growth in the planetary magnetosphere. *The Astrophysical Journal*, *904*(2), 105. https://doi.org/10.3847/1538-4357/abbeee

Zhao, J., Wang, T., Shi, C., Graham, D. B., Dunlop, M. W., He, J., et al. (2019). Ion and electron dynamics in the presence of mirror, electromagnetic ion cyclotron, and whistler waves. *The Astrophysical Journal*, *883*(2), 185. https://doi.org/10.3847/1538-4357/ab3bd1

Zhima, Z., Cao, J., Fu, H., Liu, W., Chen, L., Dunlop, M., et al. (2015). Whistler mode wave generation at the edges of a magnetic dip. *Journal of Geophysical Research: Space Physics*, *120*(4), 2469–2476. https://doi.org/10.1002/2014JA020786

Zhou, M., Deng, X., Ashour-Abdalla, M., Walker, R., Pang, Y., Tang, C., et al. (2013). Cluster observations of kinetic structures and electron acceleration within a dynamic plasma bubble. *Journal of Geophysical Research: Space Physics*, *118*(2), 674–684. https://doi.org/10.1029/2012JA018323